J|A|C|S
ARTICLES
Published on Web 04/20/2004

X-ray Magnetic Circular Dichroism of *Pseudomonas aeruginosa* Nickel(II) Azurin

Tobias Funk,*,† Pierre Kennepohl,‡ Angel J. Di Bilio,‡ William A. Wehbi,‡ Anthony T. Young,§ Stephan Friedrich,||,⊥ Elke Arenholz,§ Harry B. Gray,*,‡ and Stephen P. Cramer*,†,⊥

Contribution from the Physical Biosciences, LBNL, Cyclotron Road 1, Berkeley, California 94720; Beckman Institute, California Institute of Technology, Pasadena, California 91125; Advanced Light Source, LBNL, Cyclotron Road 1, Berkeley, California 94720; Advanced Detector Group, LLNL, Livermore, California 94550; and Department of Applied Science, University of California at Davis, One Shields Avenue, Davis, California 95616

Received May 19, 2003; E-mail: funk@lbl.gov; hbgray@caltech.edu; SPCramer@ucdavis.edu

Abstract: We show that X-ray magnetic circular dichroism (XMCD) can be employed to probe the oxidation states and other electronic structural features of nickel active sites in proteins. As a calibration standard, we have measured XMCD and X-ray absorption (XAS) spectra for the nickel(II) derivative of *Pseudomonas aeruginosa* azurin (NiAz). Our analysis of these spectra confirms that the electronic ground state of NiAz is high-spin ($S = 1$); we also find that the L_3-centroid energy is 853.1(1) eV, the branching ratio is 0.722(4), and the magnetic moment is 1.9(4) μ_B. Density functional theory (DFT) calculations on model NiAz structures establish that orbitals $3d_{x^2-y^2}$ and $3d_{z^2}$ are the two valence holes in the high-spin Ni(II) ground state, and in accord with the experimentally determined orbital magnetic moment, the DFT results also demonstrate that both holes are highly delocalized, with $3d_{x^2-y^2}$ having much greater ligand character.

Introduction

L-edge XMCD spectroscopy is a powerful spectroscopic method that can be used to investigate the differences in the metal 2p→3d absorption cross sections for right and left circularly polarized X-rays in first-row transition metals. Since the effect is dominated by the nature of the acceptor metal d orbitals, XMCD spectra are very sensitive to ligand environments and electronic structures of first-row transition metal ions,[1] and as a result, the method can be an extremely sensitive probe of oxidation and spin state.[2−4] Indeed, the technique has been used extensively in materials science and magnetism for the study of ferro- and antiferromagnetic materials;[5−8] in particular, quantitative analysis using sum rules yields magnetic parameters from integrated peak intensities.[9−12] However, the study of isolated paramagnetic species using XMCD has not been widespread, owing to experimental challenges relating to the low temperatures and high magnetic fields required.

Metalloproteins that have been studied by XMCD spectroscopy include rubredoxin,[13] plastocyanin,[14] and hydrogenase.[15] Nickel is a particularly interesting target, as it is key component of the cofactors of several functionally diverse enzymes, including urease, hydrogenase, CO-dehydrogenase, and acetyl-CoA synthase[16−19] (high-spin nickel(II) is found in hydrogenase[20] and acetyl-CoA synthase[21]). We picked a small (128

† Physical Biosciences, LBNL.
‡ California Institute of Technology.
§ Advanced Light Source, LBNL.
|| Advanced Detector Group, LLNL.
⊥ University of California at Davis.

(1) de Groot, F. M. F.; Fuggle, J. C.; Thole, B. T.; Sawatzky, G. A. *Phys. Rev. B* **1990**, *42*, 5459−5468.
(2) van der Laan, G.; Thole, B. T. *Phys. Rev. B* **1991**, *43*, 13401−13411.
(3) Cramer, S. P.; Wang, H.; Bryant, C.; Legros, M.; Horne, C.; Patil, D. S.; Ralston, C. Y.; Wang, X. In *Spectroscopic Methods in Bioinorganic Chemistry*; Solomon, E. I., Hodgson, K. O., Eds.; American Chemical Society: Washington, DC, 1998.
(4) Arrio, M. A.; Scuiller, A.; Sainctavit, P.; Moulin, C. C. D.; Mallah, T.; Verdaguer, M. *J. Am. Chem. Soc.* **1999**, *121*, 6414−6420.
(5) Stöhr, J.; Padmore, H. A.; Anders, S.; Stammler, T.; Scheinfein, M. R. *Surf. Rev. Lett.* **1998**, 1297−1308.
(6) Stöhr, J. *J. Electron Spectrosc. Relat. Phenom.* **1995**, *75*, 253−272.
(7) Gambardella, P.; Dhesi, S. S.; Gardonio, S.; Grazioli, C.; Ohresser, P.; Carbone, C. *Phys. Rev. Lett.* **2002**, *88*, 047202/1−4.
(8) Garcia, L. M.; Chaboy, J.; Bartolome, F.; Goedkoop, J. B. *44th Annual Conference on Magnetism and Magnetic Materials*; San Jose, CA, 1999; pp 6567−6569.
(9) Carra, P. *Synchrotron Radiat. News* **1992**, *5*, 21−24.
(10) Carra, P.; Thole, B. T.; Altarelli, M.; Wang, X. D. *Phys. Rev. Lett.* **1993**, *70*, 694−697.
(11) Thole, B. T.; Paolo, C.; Sette, F.; van der Laan, G. *Phys. Rev. Lett.* **1992**, *68*, 1943−1946.
(12) Wu, Y.; Stohr, J.; Hermsmeier, B. D.; Samant, M. G.; Weller, D. *Phys. Rev. Lett.* **1992**, *69*, 2307−2310.
(13) George, S. J.; Lowery, M. D.; Solomon, E. I.; Cramer, S. P. *J. Am. Chem. Soc.* **1993**, *115*, 2968−2969.
(14) Wang, H.; Bryant, C.; Randall, D. W.; LaCroix, L. B.; Solomon, E. I.; LeGros, M.; Cramer, S. P. *J. Phys. Chem. B* **1998**, *102*, 8347−8349.
(15) Wang, H.; Patil, D. S.; Ralston, C. Y.; Bryant, C.; Cramer, S. P. *J. Electron Spectrosc. Relat. Phenom.* **2001**, *114*, 865−871.
(16) Volbeda, A.; Charon, M. H.; Piras, C.; Hatchikian, E. C.; Frey, M.; Fontecillacamps, J. C. *Nature* **1995**, *373*, 580−587.
(17) Ragsdale, S. W. *Curr. Opin. Chem. Biol.* **1998**, *2*, 208−215.
(18) Maroney, M. J. *Curr. Opin. Chem. Biol.* **1999**, *3*, 188−199.
(19) Doukov, T. I.; Iverson, T. M.; Seravalli, J.; Ragsdale, S. W.; Drennan, C. L. *Science* **2002**, *298*, 567−572.
(20) Wang, H.; Ralston, C. Y.; Patil, D. S.; Jones, R. M.; Gu, W.; Verhagen, M.; Adams, M. W. W.; Ge, P.; Riordan, C.; Marganian, C. A.; Mascharak, P.; Kovacs, J.; Miller, C. G.; Collins, T. J.; Brooker, S.; Croucher, P. D.; Wang, K.; Stiefel, E. I.; Cramer, S. P. *J. Am. Chem. Soc.* **2000**, *122*, 10544−10552.

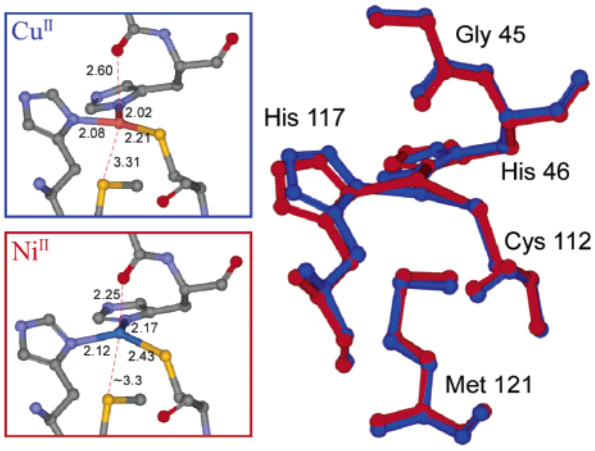

Figure 1. Cu(II) and Ni(II) sites from X-ray crystal structures of *Pseudomonas aeruginosa* azurins: PDB 1JZF[33] (at 1.5 Å) for Cu(II) and PDB 1NZR[25] (at 2 Å) for Ni(II). In both cases, the metal is slightly out of the equatorial plane defined by His46, His117, and Cys112. The oxygen atom of Gly45 is closer to the metal in the Ni(II) protein, whereas S(Met121)−Ni(II) is slightly longer than the corresponding distance to Cu(II). NMR experiments have demonstrated that the S(Met121)−Ni(II) interaction is not negligible.[29]

residues) blue copper protein,[22,23] *Pseudomonas aeruginosa* azurin, whose nickel(II) derivative (NiAz) has been structurally characterized,[24,25] as a starting point for XMCD investigations of biological nickel structures. The azurin active center is embedded in an eight-stranded antiparallel β barrel, with one extra-barrel helix inserted between β4 and β5 (numbered from the N-terminus), and both Ni(II) and Co(II) derivatives have been extensively studied.[26−30] The metal ion (Cu, Ni, or Co) is trigonally coordinated by donor atoms from the side chains of Cys112, His46, and His117 in a hydrophobic cluster at one end of the β barrel, and the Met121 thioether and Gly45 peptide carbonyl are weak axial ligands.[22,24,25,31−33] Both Ni(II) and native Cu(II) coordination geometries in the protein are shown in Figure 1.

Analysis of XAS and XMCD data confirms that the coordination complex in NiAz is highly covalent, in good agreement with ground-state density functional (DFT) calculations as well as previous experimental work.[24,26,28,29] The spin distribution over the ligands has been elucidated, and the magnitudes of the spin and orbital magnetic moments have been evaluated from both experiment and LF multiplet simulations. Importantly, our work lays a foundation for the use of L-edge XAS and XMCD experiments to probe metal oxidation states and other electronic structural features of the active sites of nickel enzymes.

Experimental Section

Sample Preparation. Azurin was expressed according to a literature procedure.[34] The crude extract was concentrated and equilibrated with 1 mM $NiSO_4$/25 mM TRIS (pH ≈ 8); nickel incorporation into apoazurin was greatly accelerated by incubating the mixture at 37 °C. NiAz was purified by FPLC and characterized by absorption spectroscopy.[26,27] Samples for XMCD experiments were in potassium phosphate buffer (pH 7).

Samples for XMCD measurements were thin films of protein deposited on sapphire disks. Typically, 15 μL of 1 mM NiAz solution formed films of about 2 μm thickness, which is comparable to the escape depth of fluorescence photons. This ensures that the fluorescence signal is maximized and that the probed volume is optimally coupled to the coldfinger of the cryostat.[35] The NiAz samples were prepared under aerobic conditions and placed in capped holders. The holders were loaded in a prechamber cooled with liquid nitrogen, transferred to the helium cooled sample stage, and uncapped. A detailed description of the sample loading procedure is available.[36]

XMCD Spectroscopy. XMCD measurements were conducted using beam line 4.0.2 at the Advanced Light Source of the Lawrence Berkeley National Laboratory. The beam line was equipped with an elliptically polarizing undulator and a high-resolution monochromator. The photon flux was 10^{12} photons/s.[37] The X-ray beam energy was calibrated against the L-edge spectrum of NiF_2 (L_3-absorption maximum at 852.7 eV).[38] The experimental setup consisted of a 6 T superconducting magnet, which hosted a sample stage attached to a separate liquid helium bath cryostat. Temperature was measured by means of a calibrated germanium resistor (Lakeshore) attached to the sample stage. The sample stage was equipped with a heat shield (cooled with liquid helium) in order to minimize heating by infrared radiation. Despite the low thermal conductivity of proteins and infrared radiation heating, we have shown that with our apparatus a temperature of 2.2 K *at sample* can be obtained.[35] The X-ray beam enters and fluorescence radiation exits the sample stage through 100 nm thick aluminum windows.

For fluorescence measurements, a Canberra 30-element germanium detector was attached to the sample chamber. With this detector (resolution ≈ 150 eV), fluorescence lines from target atoms can be distinguished from background lines. The energy of the incident X-ray photons was varied over the absorption edge. For each energy point, a fluorescence spectrum was recorded and the fluorescence lines of the investigated element integrated. These measurements yield a count rate that is proportional to the absorption cross section and are, therefore, a probe of the occupancy of the d orbitals.

EPR Spectroscopy. A sample of NiAz was analyzed by X-band EPR spectroscopy using a Bruker EMX spectrometer equipped with a helium cryostat (Oxford Instruments). The sample (50% protein dissolved in potassium phosphate buffer and 50% ethylene glycol added as cryoprotectant) was run at various temperatures in the 3.6−150 K range and at microwave power levels from a few microwatts up to 200 mW. The accessible magnetic field range was 0−1.4 T.

(21) Funk, T.; Gu, W.; Friedrich, S.; Wang, H.; Gencic, S.; Grahame, D. A.; Cramer, S. P. *J. Am. Chem. Soc.* **2004**, *126*, 88−95.
(22) Adman, E. T. *Adv. Protein Chem.* **1991**, *42*, 145−197.
(23) Gray, H. B.; Malmström, B. G.; Williams, R. J. P. *JBIC* **2000**, *5*, 551−559.
(24) Moratal, J. M.; Romero, A.; Salgado, J.; Perales-Alarcón, A.; Jiménez, H. R. *Eur. J. Biochem.* **1995**, *228*, 653−657.
(25) Tsai, L. C.; Sjölin, L.; Langer, V.; Bonander, N.; Karlsson, B. G.; Vänngård, T.; Hammann, C.; Nar, H. *Acta Crystallogr.* **1995**, *D51*, 711−717.
(26) Tennent, D. L.; McMillin, D. R. *J. Am. Chem. Soc.* **1979**, *101*, 2307−2311.
(27) Di Bilio, A. J.; Chang, T.; Malmström, B. G.; Gray, H. B.; Karlsson, B. G.; Nordling, M.; Pascher, T.; Lundberg, L. G. *Inorg. Chim. Acta* **1992**, *200*, 145−148.
(28) Jiménez, H. R.; Salgado, J.; Moratal, J. M.; Morgenstern-Badarau, I. *Inorg. Chem.* **1996**, *35*, 2737−2741.
(29) Donaire, A.; Salgado, J.; Moratal, J. M. *Biochemistry* **1998**, *37*, 8659−8673.
(30) De Kerpel, J. O. A.; Pierloot, K.; Ryde, U. *J. Phys. Chem.* **1999**, *103*, 8375−8382.
(31) Nar, H.; Messerschmidt, A.; Huber, R.; van de Kamp, M.; Canters, G. W. *J. Mol. Biol.* **1991**, *221*, 765−772.
(32) Bonander, N.; Vänngård, T.; Tsai, L. C.; Langer, V.; Nar, H.; Sjölin, L. *Proteins: Struct., Funct., Genet.* **1997**, *27*, 385−394.
(33) Crane, B. R.; Di Bilio, A. J.; Winkler, J. R.; Gray, H. B. *J. Am. Chem. Soc.* **2001**, *123*, 11623−11631.
(34) Piccioli, M.; Luchinat, C.; Mizoguchi, T. J.; Ramirez, B. E.; Gray, H. B.; Richards, J. H. *Inorg. Chem.* **1995**, *34*, 737−742.
(35) Funk, T.; Friedrich, S.; Young, A.; Arenholz, E.; Cramer, S. P. *Rev. Sci. Instrum.* **2002**, *73*, 1649−1651.
(36) Ralston, C. Y.; Wang, H.; Ragsdale, S. W.; Kumar, M.; Spangler, N. J.; Ludden, P. W.; Gu, W.; Jones, R. M.; Patil, D. S.; Cramer, S. P. *J. Am. Chem. Soc.* **2000**, *122*, 10553−10560.
(37) Young, A. T.; Martynov, V.; Padmore, H. *J. Electron Spectrosc. Relat. Phenom.* **1999**, *103*, 885−889.
(38) van der Laan, G.; Zaanen, J.; Sawatzky, G. A.; Karnatak, R.; Esteva, J.-M. *Phys. Rev. B* **1986**, *33*, 4253−4263.

Table 1. Metal−Ligand Bond Distances (Å) from NiAz Crystallographic Structures[a]

chain	O(Gly45)	N(His117)	N(His46)	S(Cys112)	S(Met121)
			S1		
A	2.26	1.97	2.22	2.54	3.28
B	2.25	2.12	2.17	2.43	3.31
C	2.30	2.17	2.00	2.55	3.32
D	2.59	2.01	2.20	2.42	3.44
av	2.35 ± 0.16	2.07 ± 0.09	2.15 ± 0.10	2.48 ± 0.07	3.34 ± 0.07
			S2		
A	2.37	2.00	2.13	2.38	3.25
B	2.43	2.03	2.15	2.25	3.35
C	2.49	2.31	2.28	2.49	3.34
D	2.57	2.54	2.37	2.43	3.25
av	2.47 ± 0.08	2.22 ± 0.25	2.23 ± 0.11	2.39 ± 0.10	3.30 ± 0.06
|av|	2.41 ± 0.13	2.14 ± 0.19	2.19 ± 0.11	2.44 ± 0.09	3.32 ± 0.06

[a] S1 (PDB 1NZR) is the structure of a Ni(II) Trp48Met mutant of azurin,[25] whereas structure S2 is that of the Ni(II) derivative of the native protein.[24] Statistical errors are reported as standard deviations over all units in the crystallographic unit cell. Structures S1-B and S2-B were chosen as representative for NiAz (see text).

DFT Calculations. DFT calculations were performed using the Amsterdam Density Functional (ADF 2002) code provided by SCM.[39−41] The Vosko, Wilk, and Nusair (VWN) local density approximation[42] was supplemented with standard nonlocal corrections from Perdew and Wang (PW91)[43] as implemented in ADF. Final results were obtained using an "all-electron" triple-ζ STO basis set (TZP basis) for all atoms. The calculations were performed by enforcing a high-spin electronic configuration ($M_s = 1$) as a single-configuration approximation to the true $S = 1$ multiconfigurational ground state.

The structure of the NiAz metal site was obtained from published crystallographic data on the Ni(II) form of the native[24] and a nonmetal site mutant (Trp48Met)[25] protein. Selected metal−ligand bond distances are given in Table 1. For each of the two crystal structures (S1 and S2), a representative single-point geometry was used to calculate the Ni(II) site electronic structure. The two geometries chosen (S1-B and S2-B) differ mainly in Ni−O(Gly) bond distances. In both cases, part of the metal site structure was truncated: His46 and His117 were represented by methylimidazoles; Met121 was represented by dimethylthioether; and Cys112 was represented by ethylthiolate (the Gly45 backbone was maintained). Details of the S1-B and S2-B DFT structural models are given as Supporting Information S1−S2. The electronic structures calculated for each model are similar. Results for the S1-B structure are reported, and those for the S2-B structure are given in the Supporting Information (including exact input files for both S1-B and S2-B).

The DFT NiAz electronic structures are reported as Mulliken charge decompositions of the resultant molecular orbitals from linear combinations of the major metal-based atomic orbitals and ligand-based molecular fragment orbitals. Details of the ligand fragment orbitals involved in bonding to the Ni(II) center are given as Supporting Information S4. Additional charge and spin decomposition schemes for the complete molecular system (multipole-derived and Hirshfeld) were used directly as implemented in ADF 2002.[39−41]

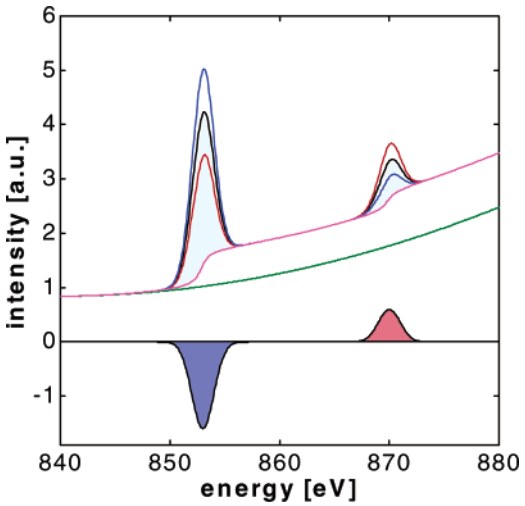

Figure 2. Schematic Ni-L-edge XAS for left (blue) and right (red) circularly polarized light. We distinguish intrinsic (pink) and parabolic (green) backgrounds. The lower curve shows the difference of the two XAS (XMCD effect). The shaded areas illustrate the integrated peak regions used in sum rule calculations: area C is in gray, A, in blue, and B, in red.

Multiplet Calculations. It is not possible at the present time to calculate full L-edge spectra for transition metal systems in the DFT framework. To determine the effect of the calculated orbital splitting on L-edge spectra, we performed LF adjusted atomic multiplet calculations. Inter- and intra-atomic interactions cause energy level splittings that account for the multiplet structure observed in XAS. Spin−orbit coupling splits the 2p shell into two sublevels $2p_{1/2}$ (lower energy level) and $2p_{3/2}$ (higher energy level), from which the L_2- and L_3-lines in L-edge spectra originate. The multiplet approach, a semiempirical method based on atomic multiplet theory, is widely used to calculate the extent of these effects on L-edge XAS.[44,45] Slater integrals and LF parameters are used as input. The atomic multiplets were calculated ab initio using the Cowan code.[2,46] LF calculations were performed using the chain of groups approach.[47]

The calculated spectra were convoluted with Lorentzian functions having $\Gamma = 0.4$ eV for the L_3-edge and $\Gamma = 0.5$ eV for the L_2-edge to account for lifetime broadening. A convolution with a Gaussian function with $\sigma = 0.2$ eV accounts for instrumental broadening.

XMCD Sum Rules. The XMCD effect is defined as the difference between spectra measured with left and right circularly polarized X-rays. Schematic spectra for left and right circularly polarized X-rays, along with the XMCD spectrum, are shown in Figure 2. The spin and orbital magnetic moments of the target atom can be derived from integrated areas pertaining to these spectra using sum rules.[9−11] The integrated areas A, B, and C used in the sum rules are indicated in Figure 2.[48] Area C, the total X-ray absorption, is defined as follows:

$$C = \frac{\mu_0 + \mu_1 + \mu_{-1}}{3}$$

in which μ_{+1} and μ_{-1} represent absorption of X-rays of right and left circular polarization, respectively, and μ_0 represents the absorption of

(39) te Velde, G.; Bickelhaupt, F. M.; Baerends, E. J.; Fonseca Guerra, C.; Van Gisbergen, S. J. A.; Snijders, J. G.; Ziegler, T. *J. Comput. Chem.* **2001**, *22*, 931−967.
(40) Guerra, C. F.; Snijders, J. G.; Te Velde, G.; Baerends, E. J. *Theor. Chem. Acc.* **1998**, *99*, 391−403.
(41) Baerends, E. J.; Autschbach, J. A.; Bérces, A.; Bo, C.; Boerrigter, P. M.; Cavallo, L.; Chong, D. P.; Deng, L.; Dickson, R. M.; Ellis, D. E.; Fan, L.; Fischer, T. H.; Guerra, C. F.; van Gisbergen, S. J. A.; Groeneveld, J. A.; Gritsenko, O. V.; Grüning, M.; Harris, F. E.; van den Hoek, P.; Jacobsen, H.; van Kessel, G.; Kootstra, F.; van Lenthe, E.; Osinga, V. P.; Patchkovskii, S.; Philipsen, P. H. T.; Post, D.; Pye, C. C.; Ravenek, W.; Ros, P.; Schipper, P. R. T.; Schreckenbach, G.; Snijders, J. G.; Sola, M.; Swart, M.; Swerhone, D.; te Velde, G.; Vernooijs, P.; Versluis, L.; Visser, O.; van Wezenbeek, E.; Wiesenekker, G.; Wolff, S. K.; Woo, T. K.; Ziegler, T. *ADF2002.01 ed.*; SCM: Amsterdam, 2002.
(42) Vosko, S. H.; Wilk, L.; Nusair, M. *Can. J. Phys.* **1980**, *58*, 1200−1211.
(43) Perdew, J. P.; Chevary, J. A.; Vosko, S. H.; Jackson, K. A.; Pederson, M. R.; Singh, D. J.; Fiolhais, C. *Phys. Rev. B* **1992**, *46*, 6671−6687.
(44) de Groot, F. M. F. *J. Electron Spectrosc. Relat. Phenom.* **1994**, *67*, 529−622.
(45) van der Laan, G. *J. Electron Spectrosc. Relat. Phenom.* **1997**, *86*, 41−47.
(46) Cowan, R. D. *The Theory of Atomic Structure and Spectra*; University of California Press: Berkeley, CA, 1981.
(47) Butler, P. H. *Point Group Symmetry Applications, Methods and Tables*; Plenum: New York, 1981.
(48) Wang, H. X.; Ge, P. H.; Riordan, C. G.; Brooker, S.; Woomer, C. G.; Collins, T.; Melendres, C. A.; Graudejus, O.; Bartlett, N.; Cramer, S. P. *J. Phys. Chem. B* **1998**, *102*, 8343−8346.

X-rays linearly polarized along the magnetization direction. Because in our experiments only μ_{+1} and μ_{-1} are measured, it is common practice to replace μ_0 by[49]

$$\mu_0 \approx \frac{\mu_1 + \mu_{-1}}{2}$$

Areas A and B are obtained by integrating the XMCD effect relative to the L_3- and L_2-lines (Figure 2). The spin and the orbital magnetic moments can be calculated using A, B, and C. The spin expectation value $\langle S_z \rangle$ is given by

$$\langle S_z \rangle = \frac{A - 2B}{2C}(10 - n_{3d})$$

in which n_{3d} is the number of electrons in the 3d orbitals of the transition metal atom. If the g factor is known, the spin magnetic moment μ_S can by calculated as follows:

$$\mu_S = -g\mu_B\langle S_z \rangle$$

The expectation value of the orbital momentum $\langle L_z \rangle$ is given by

$$\langle L_z \rangle = \frac{2(A + B)}{3C}(10 - n_{3d})$$

and since the gyromagnetic ratio for the orbital momentum is one, the orbital magnetic moment μ_L is simply[50]

$$\mu_L = -\mu_B\langle L_z \rangle$$

These formulas give the magnetic moments in units of 1/atom.

Background Correction. Spectral background correction is necessary in order to apply the sum rules. We distinguish two types of contributions to the spectral background. The intrinsic background is due to promotion of 2p electrons to vacuum and appears as a two-step-like function in the spectrum, and it is well described by the following equation:[51]

$$I_{step} = H\left[\frac{1}{2} + \frac{1}{\pi}\arctan\left(\frac{E - P}{\Gamma_L/2}\right)\right]$$

in which P is the inflection point of the step, Γ is the width of the step, and E (energy) is the independent variable. We used the maxima of the L_2- and L_3-peaks as the inflection points.[49] The second contribution originates from other atoms in the sample; this contribution was approximated by a parabolic function.

Magnetization. The quantity of interest in our measurements is the magnetic moment, which reveals the spin state and oxidation number of the target element. For paramagnets, an XMCD experiment (with the applied magnetic field along the direction of the synchrotron beam) gives the magnetization of the system. To derive the magnetic moment, however, measurement of a nearly or fully magnetically saturated sample is required. The magnetization (M) in paramagnetic compounds is a function of the strength of the applied magnetic field and temperature; for a system of N noninteracting atoms in a volume V, it is given by the following equation:[52]

$$M = \frac{N}{V}g_J\mu_B JB(x,J)$$

in which J is the total angular momentum, g_J is the electron g factor,

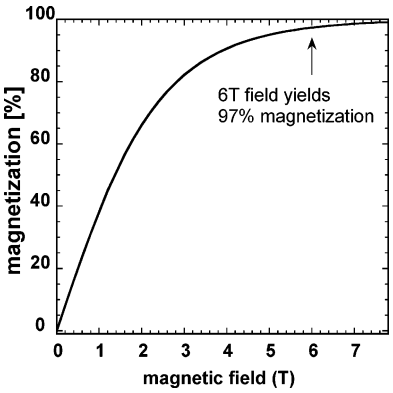

Figure 3. Magnetization curve for an $S = 1$ system assuming a sample temperature of 2.2 K. The curve is normalized to the saturation value of the magnetization.

and μ_B is the Bohr magneton. $B(x,J)$ is the Brillouin function, which is given by the following equation:

$$B(x,J) = \frac{(2J+1)}{2J}\coth\left(\frac{(2J+1)}{2J}x\right) - \frac{1}{2J}\coth\left(\frac{1}{2J}x\right), \text{ where } x = \frac{Jg_J\mu_B H}{k_B T}$$

In the pure atomic case, J can be calculated from Hund's rules. However, in a ligand field, the orbital momentum of the metal ion is partly or fully quenched.[53,54] Thus, to calculate the magnetic saturation behavior of NiAz, it is a good assumption to assume a pure spin magnetic moment, as seen from the sum rule analysis (see Table 4). The calculated magnetization curve for an $S = 1$ system is shown in Figure 3. Calculations were done assuming $T = 2.2$ K, the temperature at which the L-edge data were acquired. The magnetization was normalized to the saturation value at very high magnetic fields. The data for NiAz show 97% saturation at 6 T. Doubling the temperature decreases the degree of saturation to 82%, thereby underscoring the importance of working at very low temperatures and high fields to get meaningful results.

Radiation Damage. Sample degradation due to synchrotron radiation was assessed by acquiring L-edge spectra from the same sample spot over an extended period of time. After 2 h of beam exposure, the overall L_3-peak intensity decreased relative to the spectrum taken from a fresh spot (see S3 in Supporting Information). In addition, the low and high energy features flanking the L_3-peak merged, forming a broad peak. The intensities of the L_2-peak before and after beam exposure were comparable. The scanning procedure was optimized and sample beam exposure minimized to ensure that the data we report are for NiAz, not for a radiation-damaged material.

Results and Discussion

XAS and XMCD. NiAz L-edge spectra recorded at 2.2 K and 6 T using left and right circularly polarized X-rays are shown in Figure 4b-c; summing these spectra gives the L-edge spectrum in the absence of an external magnetic field (Figure 4a). The L_3-peak (852.7 eV) is flanked by shoulders at higher and lower energy, and a high energy peak emerges at 854.7 eV. The L_2-line (870.6 eV) is split into two components. The spectrum taken with right circularly polarized X-rays shows the same peak splitting as observed in the sum spectrum, whereas the spectrum taken with left circularly polarized X-rays has

(49) Chen, C. T.; Idzerda, Y. U.; Lin, H. J.; Smith, N. V.; Meigs, G.; Chaban, E.; Ho, G. H.; Pellegrin, E.; Sette, F. *Phys. Rev. Lett.* **1995**, *75*, 152−155.
(50) Haken, H.; Wolf, H. C. *Atomic and Quantum Physics: An Introduction to the Fundamentals of Experiment and Theory*, 2nd enl. ed.; Springer-Verlag: Berlin, New York, 1987.
(51) Stöhr, J. *NEXAFS Spectroscopy*; Springer-Verlag: New York, 1992.
(52) Ashcroft, N. W.; Mermin, N. D. *Solid State Physics*; Holt Rinehart and Winston: New York, 1976.
(53) Abragam, A.; Bleaney, B. *Electron Paramagnetic Resonance of Transition Ions*; Clarendon Press: Oxford, 1970.
(54) Pilbrow, J. R. *Transition Ion Electron Paramagnetic Resonance*; Clarendon Press: Oxford, 1990.

Table 2. Molecular Orbital Description from VWN-PW91 DFT Calculations on the NiAz S1-B Site[a]

						Ni			Met121		Cys112			His117		His46		Gly45	
	description	orbital		energy (eV)	occ up	3d	4s	4p	S_σ	S_π	SC_σ	$S_{\pi1}$	$S_{\pi2}$	N_π	N_σ	N_π	N_σ	$O_{\pi1}$	$O_{\pi2}$
→	Ni $3d_{x^2-y^2}$	111a	β	−6.283	0	54.7		0.5				3.4	34.6		2.1		2.3	0.1	0.4
→	Ni $3d_{z^2}$	110a	β	−6.577	0	77.2	1.6	1.4	0.9	5.6	0.3	6.2	0.1		0.2		0.3		5.1
→	Ni $3d_{xy}$	109a	β	−6.890	1	50.1	0.8	5.2		0.7	0.1	30.7	5.6		2.5		1.2	0.5	0.2
	C112 S_σ	111a	α	−7.268	1	22.6	1.8	4.6		11.0	0.3	42.1	11.1	0.2	2.1	0.2	0.5	0.3	0.2
	C112 S_π	110a	α	−7.445	1	10.9				5.2		9.4	68.3		1.2		0.8	0.1	
	C112 S_π	108a	β	−7.448	1	38.8		3.8	0.1	0.5		3.2	47.0		2.0		0.6		0.5
	M121 S_π	107a	β	−7.563	1	15.7	0.1	0.8	0.1	79.4			1.1		0.1		0.2	0.1	0.8
	M121 S_π	109a	α	−7.643	1	9.3	0.2	1.0	0.0	78.3	0.1	6.1	1.2	0.1	0.7		1.0	0.2	0.2
→	Ni $3d_{xz}$	106a	β	−7.823	1	78.6	0.1	0.1	0.1	9.8	1.3	0.2	2.6		0.3				1.0
→	Ni $3d_{yz}$	105a	β	−7.980	1	81.6	0.7	0.1	0.4	0.9	4.0	6.2	0.3		0.1		0.4	0.8	0.7
	C112 S_σ	103a	β	−8.354	1	48.4	2.2	1.1	0.1	1.0	4.0	29.1	2.0		0.1		0.2	2.9	
	Ni 3d	107a	α	−8.434	1	63.0	−0.1	0.5	0.1	0.0		0.9	0.6	1.9	1.6	0.8	0.5	0.3	20.5
	Ni 3d	106a	α	−8.525	1	63.5	2.5	0.9	2.4	1.6	4.7	10.2	3.2	0.7	4.8	0.2			1.2
	Ni 3d	105a	α	−8.713	1	64.9	0.4	0.3	0.8	0.5	2.6	0.6	0.2	1.4	0.6		0.5	4.9	5.7
	Ni 3d	103a	α	−8.893	1	69.8	0.1	2.4	0.6	0.2	0.6		7.6		2.1	1.3	6.7	2.8	2.6
	Ni 3d	102a	α	−9.029	1	46.1	0.3	1.2	1.1		6.2	9.3	0.5		1.7	0.5	0.9	14.4	11.9

[a] Orbitals indicated with arrows along the left-hand side are Ni $3d_\beta$. Compositions of ligand fragment orbitals are shown in Figure S4.

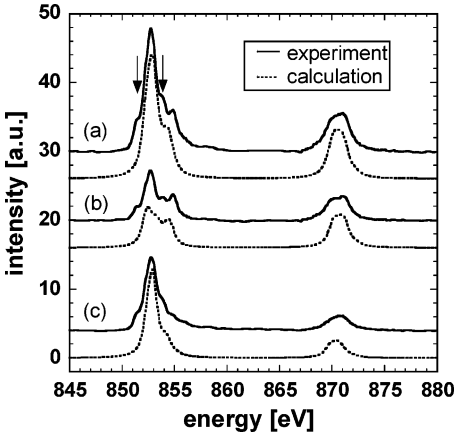

Figure 4. L-edge NiAz XAS taken with left (b) and right (c) circularly polarized X-rays; spectrum (a) shows the sum of the two contributions. Dotted lines are simulations; full lines are measured data. The arrows mark positions in the spectra that are not accounted for in the simulations.

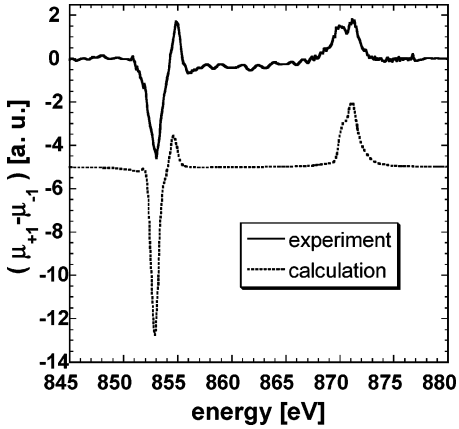

Figure 5. NiAz XMCD spectrum. Results of calculations and experiments are compared in the plot. The experimental data were corrected for polarization (the degree of polarization was 90%).

much less pronounced structure, showing essentially one peak at the L_3-edge and a less pronounced doublet at the L_2-edge. The large differences between the L-edge spectra for left and right circularly polarized light confirm that NiAz has a paramagnetic ground state.

The NiAz XMCD spectrum (corrected for the degree of polarization and for 100% saturation) is given in Figure 5. The XMCD effect shows positive and negative responses at the L_3-edge and a positive (doublet) response at the L_2-edge. The maximum effect (∼29% of the sum intensity at the respective energy) is negative and shifted ∼0.3 eV toward higher energies relative to the main peak in the sum spectrum (Figure 4a). The positive effect for the L_3-line (∼28% of the sum intensity) coincides with the second L_3-peak observed in the sum spectrum.

The oxidation state of the nickel atom can be determined from the experimental XAS by calculating the centroid energy of the L_3-line and the branching ratio for the L-edge spectrum (the branching ratio is defined as the integrated L_3-line intensity normalized by the integrated L_3- and L_2-line intensities). Cramer and co-workers have obtained XAS data for a variety of Ni(I) compounds and found an average centroid energy of 852.6 eV with a branching ratio in the range 0.73−0.78. By contrast, the average centroid energy is 853.4 eV (with $L_3/(L_2 + L_3) \approx 0.71-0.77$) for high-spin Ni(II) and 853.5 eV (with $L_3/(L_2 + L_3) \approx 0.63-0.70$) for low-spin Ni(II) compounds.[15] The L_3-centroid energy for NiAz is 853.1(1) eV (calculated using the first moment of the L_3-peak including all intensities within 80% of the maximum intensity) with $L_3/(L_2 + L_3) = 0.722(4)$, which indicates that the nickel ion is high-spin Ni(II). The spin-triplet ground-state assignment is consistent with the observed spectral splittings, which are attributable to exchange interactions.[55] Importantly, in low-spin nickel(II) compounds, only a single peak is observed.[56]

DFT Calculations. Details of the DFT molecular orbital structure for NiAz S1-B are given in Table 2. The spin-unrestricted electronic structure is described as linear combinations of metal atomic orbitals and contributing ligand fragment orbitals (vide supra). Bonding at the Ni(II) site is dominated by the two singly occupied metal 3d orbitals in the high-spin $3d^8$ configuration. The $3d_\beta$ orbital splitting (Figure 6) is that of a distorted trigonal bipyramidal site. The DFT orbital splitting is qualitatively similar to that obtained for Cu(II). We find that the magnitude of the equatorial $3d_{xy}$ and $3d_{x^2-y^2}$ orbital splitting is much smaller for Ni(II) than for Cu(II).

(55) Thole, B. T.; van der Laan, G. *Phys. Rev. B* **1988**, *38*, 3158−3166.
(56) van der Laan, G.; Thole, B. T.; Sawatzky, G. A.; Verdaguer, M. *Phys. Rev. B* **1988**, *37*, 6587−6589.

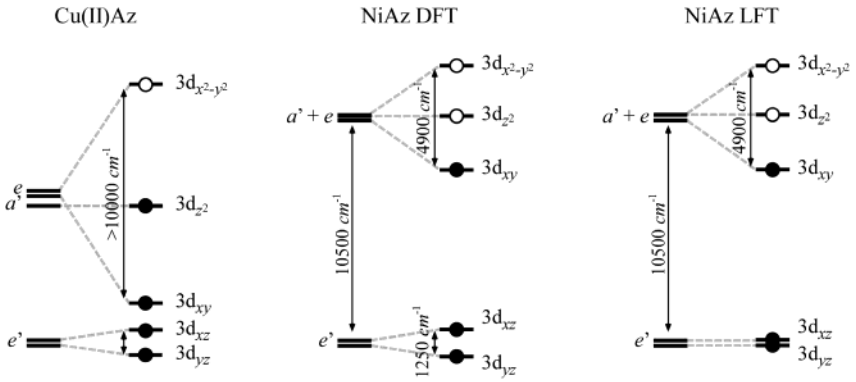

Figure 6. Metal 3d$_\beta$ orbital splitting patterns for azurin. 3d orbital splittings in native blue copper sites are those of Solomon and co-workers[57,66] (found independently by Börger et al.[65]). The NiAz 3d$_\beta$ orbital splitting from VWN-PW91 DFT calculations on the S1-B structure has been used as the starting point for LF-based multiplet simulations of the XAS and XMCD data.

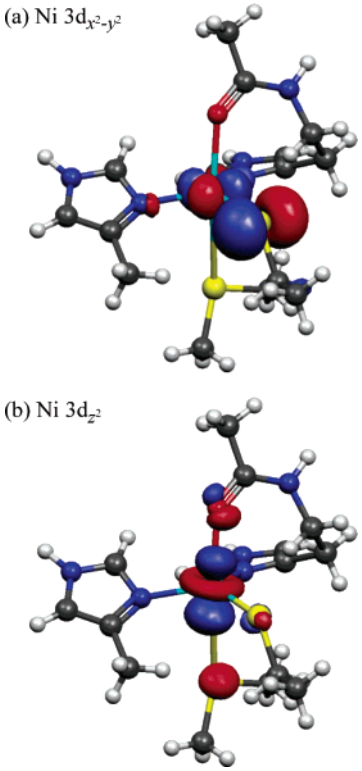

Figure 7. Graphical representation of the empty Ni 3d$_\beta$ orbitals: (a) 3d$_{x^2-y^2}$, (b) 3d$_{z^2}$. Contour isosurfaces are shown for 0.05 (e^-/Bohr^3)$^{1/2}$.

Based on the DFT orbital splitting diagram, the two holes in the 3d manifold should be in the strongly antibonding Ni 3d$_{z^2}$ and Ni 3d$_{x^2-y^2}$ orbitals (the calculated empty β-spin−orbitals are shown graphically in Figure 7). The highest energy Ni 3d$_\beta$ orbital is very similar to the SOMO of the Cu(II) protein.[57] The 3d$_{x^2-y^2}$ orbital is significantly destabilized through a strong π-antibonding interaction with a sulfur 3p orbital from the equatorial Cys112 ligand, and the orbital is further destabilized through σ-antibonding interactions with His46 and His117, which complete the equatorial plane of the trigonal site. As in the Cu(II) protein, the orbital is highly delocalized through a strong π-interaction with the cysteine ligand. The additional hole in the Ni 3d manifold is in the 3d$_{z^2}$ orbital, which is more localized than the higher energy 3d$_{x^2-y^2}$ described above. Axial ligand interactions with the 3d$_{z^2}$ involve the Gly45 backbone carbonyl oxygen at ∼2.25 Å and the Met121 sulfur at ∼3.3 Å. Contributions from these two ligands strongly depend on the Ni−O and Ni−S bond distances, as evidenced by the large difference in 3d$_{z^2}$ orbital energy in the NiAz alternative geometry (Supporting Information, Table S6). A pseudo-σ-antibonding interaction with Cys112 also is quite important in determining the overall composition of this empty 3d$_\beta$ orbital.

Table 3. Atomic and Molecular Fragment Charge (q) and Spin (s) Decomposition for the S1 Model of the NiAz Metal Site[a]

	Mulliken			Hirshfeld			multipole-derived		
fragment	q	s	$k_{av}(s)$	q	s	$k_{av}(q)$	q	s	$k_{av}(q)$
Ni	0.324	1.381	0.69	1.447	0.72	0.534	1.374	0.69	
Met121	0.137	0.060	0.03	0.062	0.03	0.105	0.061	0.03	
Cys112	−0.074	0.459	0.23	−0.581	0.21	−0.161	0.457	0.23	
His117	0.234	0.015	0.01	0.009	0.01	0.182	0.020	0.01	
His46	0.196	0.051	0.03	0.008	0.01	0.173	0.053	0.03	
Gly45	0.183	0.033	0.02	0.052	0.03	0.167	0.036	0.02	

[a] Distributions of the two holes over the metal and ligand fragments are given by k_{av} values calculated from either the charge or spin distribution.

The ligand character of each of the empty Ni 3d orbitals has been calculated using several different charge decomposition strategies (Table 3). The hole redistribution to the ligands is quite large in both the Ni 3d$_{x^2-y^2}$ and Ni 3d$_{z^2}$ orbitals, leading to a total hole count on the nickel atom of ∼1.4 from an average metal contribution of ∼0.7 in each of the two holes. The greatest charge and spin redistribution occurs between Ni(II) and Cys112, owing to both pseudo-σ- (in the 3d$_{z^2}$) and π- (in the 3d$_{x^2-y^2}$) interactions with the metal 3d orbitals. Additional contributions involve predominantly σ-type interactions with the other ligands.

Analysis

To simulate both XAS and XMCD data, we have used the parameters determined by DFT for the LF based multiplet program. The site covalency, obtained from Table 3, was used to reduce the Slater integrals in the LF calculations. The Slater integrals were systematically reduced to 80% of their ground-state atomic values due to excited-state effects[1,44,58] and were further reduced due to the covalency of the site.[58] The p−d and d−d terms were decreased to 65% and 50% of their atomic values, respectively. These atomic integral reductions correlate with ∼70% metal character (0.55/0.8) in the empty metal 3d

(57) Gewirth, A. A.; Solomon, E. I. *J. Am. Chem. Soc.* **1988**, *110*, 3811−3819.

(58) Wasinger, E. C.; de Groot, F. M. F.; Hedman, B.; Hodgson, K. O.; Solomon, E. I. *J. Am. Chem. Soc.* **2003**, *125*, 12894−12906.

Table 4. Integrated Quantities and Results from Sum Rule Analyses

NiAz	*A*	*B*	*C*	$\langle S_z\rangle/(10-n_{3d})$	$\langle L_z\rangle/(10-n_{3d})$	$\langle L_z\rangle/\langle S_z\rangle$
experiment	−7.0(6)	4.3(3)	14.6(2)	−0.53(5)	−0.12(4)	0.2(1)

Table 5. Spin and Orbital Magnetic Moments[a]

NiAz	μ_{spin}	μ_{orbit}	μ_{total}	$(10-n_{3d})^b$	g
experiment	1.7(3)	0.18(7)	1.9(4)	1.4(1)	
literature[c]			1.8		1.98

[a] Magnetic moments (in Bohr magneton units); moments are corrected for polarization (in the experiments, the degree of polarization was 90%) and extrapolated to the saturation value (measured values are at 97% saturation). [b] $(10 - n_{3d})$ as calculated by DFT. [c] Taken from ref 28.

orbitals and reflect the average DFT-calculated metal contributions to the valence holes (vide supra).

The LF parameters (10Dq 4908; Ds 1487; and Dt −708 cm^{-1}) were adjusted to reproduce the 3d orbital splitting pattern resulting from the DFT calculations based on the S1-B geometry (Figure 6 and Table 2) with the exception of the lowest lying orbitals (d_{yz} and d_{xz}), which are degenerate or slightly split (DFT) (see Figure 6). We expect that this slight difference does not affect the calculated L-edge spectra. We also performed calculations using LF parameters derived from crystal structure S2-B (10Dq 7750; Ds 1864; and Dt −491 cm^{-1}). The resulting spectra (Figure S5) resemble those shown in Figure 4 reasonably well. It is emphasized, however, that calculations using the S1-B LF parameters accord more closely with the experimental data.

An additional (exchange field) parameter is needed to describe the effect of the applied magnetic field on the XMCD spectra; the exchange field lifts the degeneracy of M_J sublevels. Because the calculations refer to a sample at 0 K, an exchange field of 80 cm^{-1} is sufficient to describe saturated magnetic moments.

The DFT-calibrated XMCD simulations reproduce the major features of the NiAz XAS and XMCD data very well. However, multiplet structure in the experimental data is more complex, yielding shoulders in L_3-spectra at lower and higher energy. These features, which are not well-reproduced in the simulations, likely reflect the strongly distorted nature of the NiAz active site, which cannot be simulated using a LF approach. Since the DFT molecular orbitals are quite different from the single-electron 3d orbitals in the multiplet approach, it is not surprising that the multiplet simulations do not fully account for the XAS features. Importantly, however, the XAS and XMCD data are very well-reproduced by the simulations, indicating that the splitting of Ni $3d_{z^2}$ and Ni $3d_{x^2-y^2}$ and their average ligand compositions are in line with the LF multiplet simulations.

The results of the sum rule analysis in Tables 4 and 5 accord well with the literature value of 1.8 μ_B obtained from magnetic susceptibility measurements.[28] One of the strengths of XMCD spectroscopy is the ability to deconvolute the orbital and spin magnetic moments. In this case, the spin magnetic moment 1.7-(3) μ_B is consistent with an $S = 1$ system. We observe a reduction of the Ni(II) orbital magnetic moment to 6% of the atomic value (3 μ_B), which is consistent with the strong covalency of the NiAz metal site revealed by our DFT analysis. In addition to an absolute value, the sum rules yield the orientation (sign) of the magnetic moments with respect to the applied magnetic field. We find that the spin and orbital magnetic moments are collinear with the applied magnetic field, in agreement with Hund's rule that *L* and *S* are coupled parallel in a more than half-filled electronic shell.

An X-band EPR spectrum was not observed for NiAz, although the search for a signal from this paramagnetic protein covered a wide temperature range.[28] The lack of a signal is consistent with a large Ni(II) zero-field splitting, one that is much greater than the microwave quantum (~0.3 cm^{-1}).[59,60] Large zero-field splittings are typical of tetrahedral [Ni(II)-N_2S_2].[61] In a study of the temperature dependence of the magnetic susceptibility of NiAz, an average *g* of 1.98 and a $|D|$[62] of 17.7 cm^{-1} were reported.[28] High-frequency EPR experiments will be required to obtain reliable spin-Hamiltonian parameters for NiAz.[63,64]

Concluding Remarks

L-edge XAS and XMCD data of *Pseudomonas aeruginosa* Ni(II) azurin confirm that the ground state is a spin-triplet ($S = 1$). The magnitude of the orbital magnetic moment further indicates that the site is highly covalent. These conclusions are well-supported by DFT calculations on model NiAz metal-site structures. From these calculations, we have shown that the two valence holes in the Ni 3d manifold are in the $3d_{z^2}$ and the $3d_{x^2-y^2}$ orbitals. Both of these orbitals are highly delocalized, although there is much greater ligand character in the one at higher energy (Ni $3d_{x^2-y^2}$).

Interestingly, the electronic structure of the Ni(II) site is qualitatively similar to that of Cu(II) in the native protein.[57,65−67] However, the splitting of the $3d_{x^2-y^2}$ and $3d_{xy}$ orbitals in Ni(II) azurin is significantly smaller, whereas the $3d_{z^2}$ energy is much higher, as is readily explained by the increased σ-antibonding character of $3d_{z^2}$, owing to the shorter M−O(Gly) bond (see Figure 1). The decreased splitting between $3d_{x^2-y^2}$ and $3d_{xy}$ probably reflects the larger Ni−S(Cys) bond distance, as the S(Cys) pseudo-σ-interaction with $3d_{xy}$ is not as strong as the π-type interaction with $3d_{x^2-y^2}$. We emphasize that the Ni(II) 3d orbital ordering is identical with that obtained experimentally for blue copper sites,[57,65,66,68] and the strong covalency of the native site is maintained. Importantly, our work on NiAz paves the way for employment of XAS/XMCD and complementary theoretical methods to elucidate the nature of nickel coordination in folded polypeptide structures.

Acknowledgment. We thank Rene Delano and the ALS staff for excellent technical support. We also thank Dr. Pieter Glatzel and Dr. Frank de Groot for helpful discussions. This work was

(59) McGarvey, B. R. *Transition Met. Chem.* **1966**, *3*, 89−201.
(60) Bencini, A.; Gatteschi, D. *Transition Met. Chem.* **1982**, *8*, 97−119.
(61) Frydendahl, H.; Toftlund, H.; Becher, J.; Dutton, J. C.; Murray, K. S.; Taylor, L. F.; Anderson, O. P.; Tiekink, E. R. T. *Inorg. Chem.* **1995**, *34*, 4467−4476.
(62) For a standard $S = 1$ spin-Hamiltonian, $D = -3/2 D_{zz}$; D_{zz} is the *z* component of the diagonal dipolar tensor (Wertz, J. E.; Bolton, J. R. *Electron Spin Resonance*; Wiley: New York, 1994).
(63) Krzystek, J.; Park, J. H.; Meisel, M. W.; Hitchman, M. A.; Stratemeier, H.; Brunel, L. C.; Telser, J. *Inorg. Chem.* **2002**, *41*, 4478−4487.
(64) Ubbink, M.; Worrall, J. A. R.; Canters, G. W.; Groenen, E. J. J.; Huber, M. *Annu. Rev. Biophys. Biomol. Struct.* **2002**, *31*, 393−422.
(65) Börger, B.; Gutschank, J.; Suter, D.; Thomson, A. J.; Bingham, S. J. *J. Am. Chem. Soc.* **2001**, *123*, 2334−2339.
(66) LaCroix, L. B.; Shadle, S. E.; Wang, Y.; Averill, B. A.; Hedman, B.; Hodgson, K. O.; Solomon, E. I. *J. Am. Chem. Soc.* **1996**, *118*, 7755−7768.
(67) Olsson, M. H. M.; Ryde, U. *JBIC* **1999**, *4*, 654−663.
(68) The 3d orbital ordering for blue copper active sites obtained using theoretical methods is inconsistent with that which has been observed through experimental methods. This has led to some confusion about the similarities and differences between CuAz and NiAz (see ref 29).

supported by NIH (GM4430 and DK19038) and the U.S. Department of Energy (Office of Biological and Environmental Research).

Supporting Information Available: (**S1**) Geometric structure and ADF input information for NiAz S1-B calculations. (**S2**) Alternative geometric structure of NiAz S2-B (longer Ni−O axial bond distance); all results from this calculation are given as Supporting Information. (**S3**) Spectrum showing the effect of X-ray irradiation on the L_3-peak of NiAz. (**S4**) Important ligand fragment orbitals for Met121, Cys112, His117, His46, and Gly45. (**S5**) Calculated spectra for NiAz structure S2-B. (**S6**) DFT results for NiAz structure S2-B. (**S7**) $3d_\beta$ orbital splitting diagram for NiAz structure S2-B. This material is available free of charge via the Internet at http://pubs.acs.org.

JA036218D